Basal Sliding and Hydrological Drainage at Baltoro Glacier

Anna Wendleder[1], Jasmin Bramboeck[2], Jamie Izzard[3], Thilo Erbertseder[1], Pablo d'Angelo[4],
Andreas Schmitt[2], Duncan J. Quincey[3], Christoph Mayer[5], and Matthias H. Braun[6]

[1]German Remote Sensing Data Center, German Aerospace Center, Oberpfaffenhofen, Germany
[2]Institute for Applications of Machine Learning and Intelligent Systems, Munich University of Applied Sciences, Munich, Germany
[3]School of Geography, University of Leeds, Leeds, UK
[4]Remote Sensing Technology Institute, German Aerospace Center, Oberpfaffenhofen, Germany
[5]Geodesy and Glaciology, Bavarian Academy of Sciences and Humanities, Munich, Germany
[6]Institut für Geographie, Friedrich-Alexander-Universität Erlangen-Nuremberg, Erlangen, Germany

Correspondence: Anna Wendleder (anna.wendleder@dlr.de)

Abstract. Surface meltwater directly influences glacier velocity, as liquid water at the bed allows the glacier to slide. However, prolonged discharge of water at the bed increases the efficiency of the drainage system and decreases the amount of sliding. Due to the presence of an insulating debris mantle, debris-covered glaciers respond in a more complex way to changes in climate than those that are debris-free. The influence of long-lasting high temperatures on melt processes and, subsequently, supraglacial lake formation, and the triggers of basal sliding have not yet been sufficiently analyzed and understood. We present a spatio-temporal analysis of key glacier characteristics for the Baltoro Glacier in the Karakoram, from October 2016 to September 2022 based on Earth Observation data and climate parameters extracted from the High Asia Refined analysis (HAR) data set. For the glacier variables, we used surface velocity, supraglacial lake extent, snowmelt, and runoff derived from Earth Observation data. For climate variables, we focused on air temperature and precipitation. The relationship and dependency between the variables were examined with Pearson correlation and linear regression, respectively. Additionally, the temporal delay between snowmelt peak and glacier flow acceleration was determined. The surface velocity of the Baltoro Glacier was characterized by a spring speed-up, summer peak, and fall speed-up with the largest increase in spring of 1.0-1.7 m d⁻¹ triggered by the onset or an increase of basal sliding. Snowmelt has the largest impact to the spring speed-up, summer velocity peak, and to the transition from inefficient to efficient drainage. It covered up to 64 % (353 km²) of the complete (debris-covered and debris-free) Baltoro Glacier and reached up to 4700 m a.s.l. during the first melt peak and up to 5600 m a.s.l. during summer. The temporal delay between the initial peak of seasonal snowmelt and the first relative velocity maximum decreases downglacier. Drainage from supraglacial lakes (3.6-5.9 km²) contributed to the fall speed-up, which showed a lower magnitude by 0.1-0.2 m d⁻¹ than the summer velocity peak. Most of the runoff can be attributed to snowmelt. However from mid-June onwards, the lakes play an increasing role, even though their contribution is estimated to be only about half of that of the snowmelt. The observed increase in summer temperatures influences the magnitude of snowmelt, as well as the formation of supraglacial lakes. This tendency is expected to intensify in the future.

1   Introduction

Glacial meltwater is an important control over the glacier dynamics. In particular, the seasonal evolution and variation of glacier flow is strongly influenced by the timing and amount of meltwater (Glasser, 2013; Iken and Bindschadler, 1986).

25   With the melt onset, surface melt water is formed and possibly drains to the glacier bed via crevasses or englacial pathways and is stored in cavities and distributed channels (Röthlisberger, 1972; Cuffey and Paterson, 2010). This influx of meltwater into the subglacial drainage system leads to an increase in basal water pressure. When subglacial water pressure approaches ice-overburden pressure, basal traction decreases and sliding is initiated as the ice decouples from the bed, the glacier lifts up and accelerates (Weertman, 1964; Lliboutry, 1968; Iken and Bindschadler, 1986; Nolan and Echelmeyer, 1999; Sugiyama

30   et al., 2011; Hoffman et al., 2016; Benn et al., 2019). Additionally, the inflow of water through inefficient channels generates frictional heat which melts the ice walls and thus expands the channels leading ultimately to the formation of an efficient drainage system (Röthlisberger, 1972; Flowers, 2015). In an efficient channel system, water storage is reduced and water pressure in the channels lessens and glacier flow velocity decreases (Benn et al., 2019). In the absence of meltwater the ice-overburden pressure is larger and leads hence to a closure of the channels through regelation and creep (Benn et al., 2019;

35   Flowers, 2015; Jiskoot, 2011). Glacier movement is responding to driving stress, a function of ice thicknesses and surface slope, and can be divided into the three flow processes of ice deformation, basal sliding, and sediment deformation. Sliding and bed deformation occur only in the case of temperate and polythermal glaciers. In this way, basal sliding and bed deformation (if existent) can contribute up to 50 % of the total glacier surface velocity with magnitudes greater than internal deformation velocities (Boulton and Hindmarsh, 1987; Jiskoot, 2011).

40   Glacier speed-ups in spring (Mair et al., 2001; Macgregor et al., 2005; Nanni et al., 2023), summer (Iken and Bindschadler, 1986; Copland et al., 2003; Bartholomaus et al., 2008; Quincey et al., 2009; Hewitt, 2013; Werder et al., 2013; Van Wychen et al., 2014; Armstrong et al., 2017; Nanni et al., 2023; Rada Giacaman and Schoof, 2023) and winter (Burgess et al., 2013; Hart et al., 2022) have widely been observed and their changes linked to an increase of temperatures, surface melt, and subglacial hydrology. In the case of debris-free glaciers, meltwater creation can be directly associated with warmer air temperatures and

45   surface melt. Debris-covered glaciers, however, have a more complex, non-linear ablation with enhanced melting in areas of thin debris cover (few centimeters), thermal insulation in areas of thick debris coverage (Østrem, 1959; Nicholson and Benn, 2006), and melting hot-spots at ice cliffs (Brun et al., 2018; Buri et al., 2021) and supraglacial lakes (Miles et al., 2020). The supraglacial lake discharge can support basal sliding and hence higher glacier velocities (Sakai and Fujita, 2006; Sakai, 2012; Watson et al., 2016; Benn et al., 2017; Miles et al., 2020). Previously, we presented a time series of annual and seasonal

50   glacier surface velocities derived from multi-mission Synthetic Aperture Radar (SAR) data for Baltoro Glacier, located in the Karakoram, Pakistan, from 1992 to 2017 (Wendleder et al., 2018). We could show that in some years, the acceleration lasted longer and affected a larger glacier area than in others. In years with higher velocities, the supraglacial lakes mapped from Landsat and ASTER imagery were characterized by a larger number and a larger total area as well. However, only one image for each summer was available for mapping and did not provide sufficient insight into the seasonal evolution of the

55   supraglacial lakes or their link to surface velocity. Therefore, we developed an approach using multi-temporal and multi-sensor

Earth Observation data to provide a dense, almost daily summer time series of supraglacial lakes (Wendleder et al., 2021a). Nevertheless, there is still a lack of detailed process understanding whether and how the development of supraglacial lakes triggers basal sliding.

In this study, we combined relevant glacier variables derived from Earth Observation data and climate records to assess the extent to which the Baltoro Glacier responds, spatially or temporally, to a given climatic forcing. The processes and relationship of the variables were examined by statistical analysis. For the glacier variables, we used 1) surface velocity derived by intensity offset tracking from Sentinel-1 time series, 2) supraglacial lakes mapped by a random forest classifier applied on Sentinel-2, PlanetScope, Sentinel-1, and TerraSAR-X data, 3) snowmelt detected using a change detection algorithm based on Sentinel-1, and 4) runoff estimated as surface areal coverage from Sentinel-2 and PlanetScope imagery. For the climate variables we focussed on air temperature and precipitation extracted from the High Asia Refined analysis (HAR) data set. The analysis focused on the period from October 2016 to September 2022 providing a dense and continuous time series.

2 Study site

The Baltoro Glacier is located in the eastern Karakoram in the northern part of Pakistan (Figure 1). The glacier has a length of about 63 km and, together with its tributary glaciers, covers an area of approximately 554 km^2. Above Concordia (4600 m a.s.l.), the two major tributaries Godwin Austin Glacier and Baltoro South Glacier converge to the main Baltoro Glacier and change their flow direction westward. Several major tributary glaciers merge with the main branch along its northern and southern margins (Mayer et al., 2006; Quincey et al., 2009). Surface velocities range between 0.5 to 0.65 m d^{-1} in summer and 0.3 to 0.4 m d^{-1} in winter between Concordia and Urdukas (3900 m a.s.l.), and decrease to 0.03 to 0.1 m d^{-1} near the terminus at 3400 m a.s.l. (Quincey et al., 2009; Wendleder et al., 2018). Approximately 38 % of the Baltoro Glacier is debris covered with a thin layer of 5-15 cm at Concordia, 30-40 cm at Urdukas, and in the order of 1 m thickness near the glacier terminus (Mayer et al., 2006; Quincey et al., 2009). Debris-covered glaciers are characterized by the presence of ice cliffs (Mayer et al., 2006; Evatt et al., 2017) and supraglacial lakes (Wendleder et al., 2021a). On the Baltoro Glacier ice cliffs are found between the terminus and Gore. Supraglacial lakes are located on the main glacier from the terminus up to Concordia. They usually fill between mid-April to mid-June and drain between mid-June to mid-September.

The Karakoram has a mid-latitude high-mountain climate with cold winters and mild summers. The regional climate is influenced by winter westerly disturbances with dominant winter and spring snowfall (Mayer et al., 2014; Dobreva et al., 2017), Indian summer monsoon with higher liquid precipitation, temperatures, and cloud coverage (Thayyen and Gergan, 2010; Bookhagen and Burbank, 2006), and the predominantly stable Tibetan Anticyclone. In the case of an irregular weakening and thus causing an incursion of the Indian summer monsoon, large amounts of summer precipitation can be observed (Dobreva et al., 2017). The climate variables are strongly determined by the topography. Hence, precipitation increases with altitude reaching a mean annual rate of approximately 1600 mm pear year at 5300 m a.s.l. (Godwin Austen region) and at 5500 m a.s.l. (Baltoro South region). The average daytime temperature during summer is close to the freezing point at 5400 m a.s.l., consequently most of the precipitation deposits as snow above this elevation (Mayer et al., 2006).
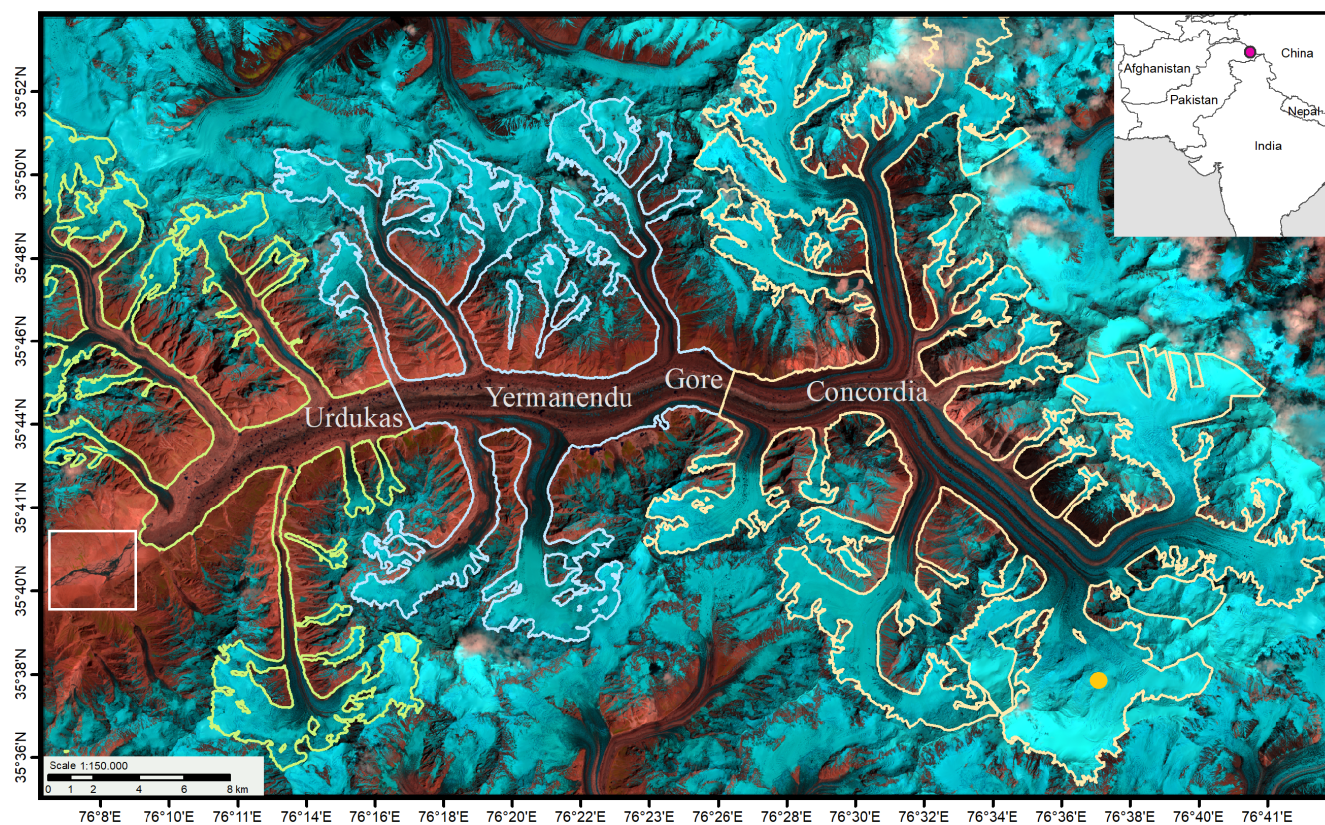
Figure 1. Overview of the Baltoro Glacier, Pakistan. Important place names are indicated. The area of the mapped runoff is displayed with a white rectangle. The western, central, and eastern sector for the snowmelt mapping is displayed in green, blue, and orange. The air temperature was extracted at Urdukas and the precipitation at Baltoro South Glacier which is marked with a yellow point (center of the HAR pixel). The background image is a Sentinel-2 composite (shortwave-infrared, near-infrared, red) acquired on 22 July 2019.

3 Material and Methods

90 This chapter describes the used Earth Observation data, known methods to process them into level-2 data, and the used reanalysis data. Furthermore, the analyses of the spatio-temporal relationship of the variables, the Pearson correlation and the linear regression to quantify the direction and strength of the relationship and the dependency are explained.

3.1 Glacier surface velocity

The glacier surface velocity was calculated from the Sentinel-1 Interferometric Wide Swath Single Look Complex (SLC) data.
95 We used only data from the ascending orbit as only these were continuously available for the complete observation period. The intensity offset tracking algorithm was applied to consecutive pairs of co-registered SAR intensity images (Strozzi et al., 2002; Friedl et al., 2018). Tracking patch sizes and step sizes were adapted to sensor specifications and expected displacement lying at

250 x 50 pixel and 50 x 10 pixel, respectively. The Copernicus Digital Elevation Model (DEM) (1 arc second, version 2022_1, (ESA, 2019)) provided the topographic reference for geocoding and orthorectification of the surface velocity maps. The mean accuracy of the velocity maps is 0.06 m d^{-1} of a pixel resulting in a standard deviation of 0.042 m d^{-1} (Strozzi et al., 2002; Friedl et al., 2021). For the analysis, we extracted the surface velocity values along the glacier centerline at four different locations, namely at Urdukas (11 km), at the confluence with Yermanendu Glacier (16 km), Gore (23 km), and Concordia (33 km distance from terminus). The four different points were selected to best reflect the spatial variation along the glacier.

3.2 Supraglacial lake mapping

Supraglacial lakes were mapped based on a multi-sensor and multi-temporal summer time series from 2016 to 2022 acquired by the optical sensors Sentinel-2 and PlanetScope as well as the SAR sensors Sentinel-1 and TerraSAR-X. The Sentinel-2 Multi Spectral Instrument (MSI) orthorectified Level-1C Top-Of-Atmospheric products were atmospherically corrected to L2A products using MAJA (MACCS ATCOR Joint Algorithm, release 4.2, (Hagolle et al., 2017)). The PlanetScope Analytic Ortho Scene Products (Level 3B) were downloaded as orthorectified and atmospherically corrected Surface Reflectance (SR) data. In our approach, a coregistration of the PlanetScope data is not needed since the assignment of the classified lakes over the season is performed using their center coordinate. Sentinel-1 Interferometric Wide Swath Single Look Complex (SLC) C-band and TerraSAR-X ScanSAR Multi-Look Ground Range Detected (MGD) X-band data were processed to Analysis Ready Data (ARD) using the Multi-SAR System (Schmitt et al., 2015, 2020). The mapping of the seasonal lake evolution used a semi-automatic approach which is based on a random forest classifier applied separately to each sensor. To produce a consistent and internally robust time series, a combination of linear regression and the Hausdorff distance (Hausdorff, 1914) were used to harmonize SAR- and optical-derived lake areas. The time series has a temporal sampling of 2-4 days with a spatial sampling of 10 m. The mean relative Root Squared Error is at 1.0 % (total area of 9.151 km^2 with an absolute RSE of 0.0945 km^2). Detailed processing steps and results for the years 2016 to 2020 were published by Wendleder et al. (2021b). For this study, the time series was extended by 2021 and 2022.

3.3 Glacier runoff mapping

Since we only had Earth Observation data available, we were limited to mapping the width of the glacier discharge and using the estimated surface areal coverage as proxy of the quantitative runoff given in km^2. To avoid misunderstanding to conventional runoff measurements given in volume, we are using the term 'runoff-index'. The mapping was only applied to the area of the upper runoff course (2.7 km^2 area and 5.6 km length) bordered to south and north by alluvial fans and slopes (see white rectangle in Figure 1). From the low-flow to peak discharge period, the water-filled channel area at the glacier's terminus width increased tenfold from 70 m to around 700 m. We used the Sentinel-2 Multi Spectral Instrument (MSI) orthorectified and MAJA atmospherically corrected L2A products and the PlanetScope Analytic Ortho Scene Products (Level 3B) Surface Reflectance (SR) data. Due to the high turbidity of the glacier discharge, water and sandy soil are hard to differentiate using the Normalized Different Water Index. Therefore, the optical data of each sensor were first fused to Kennaugh Elements using the red, green, blue, and near-infrared bands. In radar, the Kennaugh Elements describes the polarimetric information and

enables the interpretation of physical scattering mechanisms. In the case of optical data, the Kennaugh Elements are a fusion technique to combine multiple multi-spectral bands to one image while enhancing their spectral characteristics (Schmitt et al., 2020). Afterwards, a K-means clustering grouped each image into the two classes "runoff" and "background". The classes were assigned geographically using a point in the confluence after the delta that was always covered with water. Compared to the

135   manually digitized reference based on the near-infrared band, the classification achieved a mean relative RSE of 0.12 % (total area of 3.1 km^2 with an absolute RSE of 0.14 km^2). The time series has a temporal sampling of 5-15 days at the beginning of the ablation season which is characterized by a higher cloud coverage and 1-5 days during the ablation season with less cloud coverage.

3.4   Snowmelt mapping

140   We mapped the wet snow on the complete Baltoro Glacier which includes the debris-covered and debris-free part of the glacier from the Sentinel-1 Interferometric Wide Swath C-band data. The processing of the SLC to ARD data was performed with the Multi-SAR System (Schmitt et al., 2020). The additional use of image enhancement (specifically, multi-scale multi-looking) resulted in a smoothing of noise and hence a more homogeneous environment and a better wet snow classification (Schmitt et al., 2015; Wendleder et al., 2022). As cross-polarisation (VH) has a greater absorption over wet snow, leading to a lower

145   backscatter and hence a better discrimination of wet snow (Rott and Mätzler, 1987), we used only this polarization. For every scene, the image difference to a reference scene was calculated. To ensure cold temperatures prevailed during the acquisition, the first scene in January of each year, the coldest month, was chosen as the reference scene. As threshold we used one half of the signal power (-3 dB) (Shi and Dozier, 1995; Nagler and Rott, 2000; Scher et al., 2021). By intersecting the wet snow mapping with the Copernicus DEM (1 arc second, version 2022_1, (ESA, 2019)), the aggregated area between the 10 % and

150   90 % percentile of the elevation was used. We selected only SAR acquisitions from the ascending orbit. Firstly, the ascending images were acquired during the afternoon (13:00 UTC, 18:00 local time) to better represent the maximum melt area than the descending images acquired during the morning (1:00 h UTC, 6:00h local time). Secondly, the accumulation areas of the tributary glaciers were imaged with only minor influence of layover or radar shadow as the slopes faced away from the sensor (Wendleder et al., 2021a). The wet snow mapping product has a temporal resolution of 12 days. For the snowmelt mapping,

155   we divided the glacier into the western (from glacier terminus to Urdukas), central (from Urdukas to Gore), and eastern area (upwards of Gore). As area and elevation of the glacier increases from west to east, the classification reflects the vertical gradient and hence the temporal delay.

3.5   Air Temperature and Precipitation

The near surface temperature and total precipitation data were obtained from the daily interpolated HAR data set (version 2)

160   provided by Chair of Climatology, TU Berlin. The Weather Research and Forecasting (WRF) model was dynamically downscaled to this regional atmospheric data set based on European Centre for Medium-Range Weather Forecasts (ECMWF) Re-Analysis (ERA-5). HAR is available for the period 1980 to 2022 (Wang et al., 2021). The elevation model used for the downscaling with its spatial resolution of 10 km is too coarse to represent the complex terrain of the Karakoram, which leads

to an underestimation of temperatures in the lower glacier and an overestimation of temperatures on the accumulation area. To
165 downscale the temperatures, a monthly mean lapse rate was determined on basis of a fitting curve (3rd order) using data from
an automatic weather station located at Urdukas. The lapse rates varied between 7° C and 11° C km^{-1}. The precipitation was
extracted at Baltoro South Glacier, one of the two major tributaries with the larger glacier area.

3.6 Temporal relationship

The first step is to analyse if there is a temporal relationship between the supraglacial lakes, snowmelt, glacier velocity, runoff-
170 index, air temperature, and precipitation. For the presentation, we plotted all variables in one figure using the hydrological year
(1 October-30 September) as time reference.

3.7 Spatial relationship

If the temporal representation shows a relationship in time between the variables supraglacial lakes, snowmelt, and glacier
velocity, the spatial representation demonstrates if the variables are spatially related as well, i.e. whether the location of drainage
175 and velocity are nearby. Therefore, glacier velocity was displayed on a hexagonal grid known as H3. The advantage of a
hexagonal compared to a rectangular grid is the simpler and more symmetric nearest neighborhood and the better clarity in
visualizations. The conversion from the rectangle to hexagonal presentation is based on resampling using the median value.
Only the supraglacial lakes that arose or drained in the observed period of higher glacier velocity were displayed in order to
analyze if the draining water could be a control on ice dynamics.

180 ### 3.8 Pearson Correlation

The glacier surface velocities were correlated with the supraglacial lake area, snowmelt extent, runoff-index, and meteoro-
logical parameters. As each variable had a different temporal resolution, the time series were resampled to daily values. The
Pearson correlation was applied each year for two different periods: 1) the first period was defined from the day with the first
positive air temperatures at Urdukas until the time of maximum glacier velocity and 2) the second period from the time of
185 maximum glacier velocity until the end of the ablation season on 30 September (Berthier and Brun, 2019). The significance
of the correlation coefficients with a confidence level of 95 % was estimated using the student distribution (Obilor and Amadi,
2018).

3.9 Linear Regression

To analyze the relationship between the datasets as well as the dependency of all variables for both periods separately, we
190 applied a linear regression based on a least-square robust adjustment using R^2 and the regression coefficient (slope) to show
the dependency of the variables. The significance of any observed trends was estimated using the Mann–Kendall test with a
confidence level of 95 %.

4 Results

First, we present the results of the spatio-temporal relationship, followed by the results of the Pearson correlation, linear
195 regression, and the estimated temporal delay between snowmelt and surface velocity.

4.1 Temporal relationship

The temporal relationship of the supraglacial lakes, runoff-index, surface velocity, air temperature, precipitation, and snowmelt
for October 2016 to September 2022 is shown in Figure 2. Table 1 lists the glacier and climate variables and their relevant
parameters. During March (earliest: 5 March 2022, latest: 27 March 2019), temperatures consistently rose into the positive
200 range for the first time. In mid-April there was usually a period of higher temperatures, coinciding with a preceding precipitation
event. At this time, the snowmelt line and the zero degree level (estimated from the temperatures at Urdukas) was at 4700 m
a.s.l., hence the precipitation above that altitude fell as snow. Afterwards, snowmelt area and air temperatures exhibited a linear
relationship which indicated that higher temperatures were present in higher altitudes. Spring 2022 was significantly affected
by heat waves (Otto et al., 2023). In summer 2022, the degree day sum at Urdukas was at 2084 compared to value range of
205 1822 (2019) and 1989 (2017) which led to an early supraglacial lake peak (28 May).

The snowmelt started on 27 March (earliest; 2019) and 21 April (latest; 2021) and terminated at the end of October. First the
snow melted in the lower altitudes (3600-4300 m a.s.l.) on the debris-covered main branch and debris-free tributary glaciers,
later only on the debris-free glaciers in the higher altitudes (up to 4700 m a.s.l.). The snowmelt fluctuated gradually through
time between minimum and maximum extent, reaching spatial maxima of 90 km^2 for the western sector (2018), 84 km^2 for
210 the central sector (2017), and 190 km^2 for the eastern sector (2019). In July 2019, the total snowmelt area had a maxima of
353 km^2 covering only the debris-free part of the glacier. It corresponds to 64 % of the total area of Baltoro Glacier. A temporal
delay from the lower (west) sector to the upper (east) sector was hardly discernible. Differences only existed in the snowmelt
area as the east sector covers a larger glacier area than the western and central sector.

The maximum area of the supraglacial lakes ranged between 1.9 km^2 (2019) and 3.1 km^2 (2022). The consistent character-
215 istic for all six years was a fast formation at the beginning and a slow drainage at the end of the ablation season. The peak was
reached from end-May/early-June (2020, 2022) through mid/end-July (2017, 2018, 2019) to mid-August (2021). In 2020, the
lake evolution was characterized by a second peak from early-September to mid-September.

The winter surface velocities (1 October until the first date with positive temperatures usually at the beginning/end of
March) ranged over the years between 0.05 and 0.37 m d^{-1} with values around 0.05-0.15 m d^{-1} at Urdukas and values above
220 0.15 m d^{-1} upstream of Yermanendu. The velocities at Urdukas and Concordia varied by 0.1 and 0.16 m d^{-1} during this period,
respectively. The low winter velocities were followed by a spring speed-up. This event lasted usually from the end of April
to the beginning of May and led to an increase of 0.1–0.16 m d^{-1} above Yermanendu. In 2017, 2019, 2020, and 2021, the
velocities at Gore exceeded even those at Concordia at this time. The spring speed-up was particularly visible in 2018 affecting
all four locations. Though, in 2022, the velocities at Urdukas were rarely impacted. After the speed-up, the flow at Concordia
225 accelerated continuously until the summer peak of 0.46-0.59 m d^{-1} was reached in June to July. Only in 2022, a short slow-
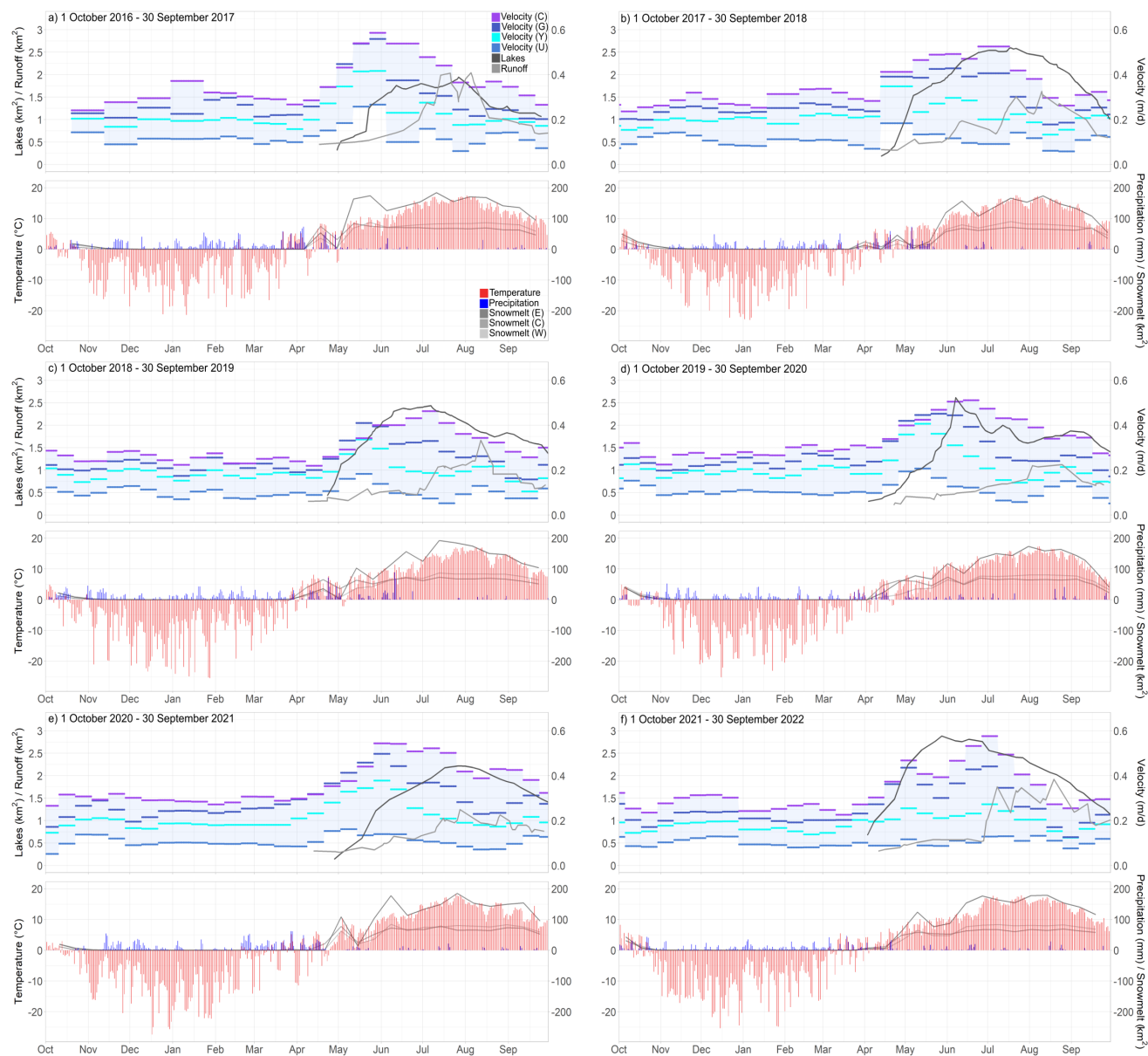
Figure 2. Temporal relationship of the supraglacial lakes, runoff-index, surface velocity, air temperature, precipitation, and snowmelt for 1 October 2016 to 30 September 2022 (a-f). All images have the same legend shown in a). The label of the left y-axis is displayed on the outer left side, that of the right y-axis on the outer right side. The abbreviation U stands for Urdukas, Y for Yermanendu, G for Gore, and C for Concordia (surface velocity) whereas W stand for western, C for central, and E for eastern sector (snowmelt).

Table 1. Glacier and climate variables with their relevant parameters for October 2016 to September 2022. The abbreviation W stand for western, C for central, and E for eastern sector.

	Oct 2016–Sept 2017	Oct 2017–Sept 2018	Oct 2018–Sept 2019	Oct 2019–Sept 2020	Oct 2020–Sept 2021	Oct 2021–Sept 2022
Surface Velocity						
Winter Velocity (m d⁻¹)	0.09-0.37	0.08-0.33	0.07–0.29	0.08–0.33	0.05–0.32	0.08–0.32
Period of Winter Velocity	20 Oct-17 April	1 Oct–12 April	1 Oct–12 April	1 Oct–12 April	1 Oct–12 April	1 Oct–12 April
Spring Speed-up Velocity (m d⁻¹)	0.15-0.54	0.34-0.41	0.41	0.45	0.46	0.47
Period of Spring Speed-up	18 April-23 May	13 April–7 May	2 May–25 May	26 April–19 May	21 April–26 May	28 April–9 May
Peak Velocity (m d⁻¹)	0.59	0.53	0.46	0.51	0.54	0.58
Period of Peak Velocity	24 May-4 June	26 June-18 July	1 July–12 July	13 June–24 June	27 May–19 June	27 June–8 July.
Fall Speed-up Velocity (m d⁻¹)	0.37	0.32	0.33	0.34	0.43	0.32
Period of Fall Speed-up Velocity	16 Aug-27 Aug	4 Sept-27 Sept	23 Sept–16 Oct	5 Sept–16 Sept	19 Aug–30 Sept	19 Sept–30 Sept
Supraglacial Lake						
Number of Lakes	412	501	498	379	372	710
Aggregated Area (km²)	1.9	2.6	2.4	2.0	2.5	2.9
Cumulative Area (km²)	3.6	5.8	4.7	4.6	4.8	5.9
Date of Peak	28 July	23 July	8 July	12 July	11 Aug	28 May
Runoff-Index						
Date of Peak (Area (km²))	21 July (2.1) 5 Aug (2.0)	12 June (1.0) 22 July (1.5) 10 Aug (1.6)	22 May (0.6) 16 July (1.1) 12 Aug (1.7)	3 Aug (1.1) 25 Aug (1.1)	10 June (0.6) 28 July (1.2) 26 Aug (1.1)	16 June (0.6) 8 July (1.8) 26 July (1.7) 19 Aug (1.9)
Cumulative Area (km²)	36.0	32.0	27.7	17.0	31.4	27.3
Snowmelt						
Period	18 April-26 Dec	1 April-22 Oct	27 Marc–28 Dec	14 April–16 Nov	21 April–17 Dec	4 April–24 Dec
Total max. Area (km²)	336	328	353	319	335	326
max. Area per W/C/E Sector (km²)	87/84/184	90/72/173	87/73/193	81/74/174	85/79/185	84/69/179
Total annual Area (km²)	3697	2989	3697	3701	3551	3773
Temperature						
Degree Day Sum (°C)	1989	1890	1822	1851	1911	2084
Period with pos. temperatures	21 March–22 Oct	12 Marc-1 Nov	27 March-30 Oct	21 March-28 Oct	7 March-22 Oct	05 March-5 Nov
Precipitation						
Winter Period (mm)	3664	2621	3514	3128	3358	2670
Summer Period (mm)	1468	1658	1754	1234	1088	914

down between the speed-up and the summer peak was recognizable. The high lasted for 11-12 days in 2017, 2019, 2021, and 2022 and 22 days in 2018 and 2020. However, not all four locations experienced the maximum velocity at the same time: in 2022, the summer peak affected all four locations; in 2021, only the area upglacier of Yermanendu was influenced; in 2020 and 2019, the velocities downglacier of Gore reached their maximum during the spring speed-up; in 2018, the velocities

230 at Concordia and Gore had their high during summer peak, Yermanendu and Urdukas during spring speed-up; in 2017, the velocities upwards of Yermanendu reached their maximum during summer peak and Urdukas afterwards. Additionally, the year 2021 was characterized by a continuous transition of spring speed-up and summer peak. Afterwards, the values between Concordia and Urdukas spread with a difference of up to 0.46 m d^{-1}. In 2017 and 2021, this phenomenon happened after the summer peak and in 2018-2020 between speed-up and summer peak. After the summer peak, the ice decelerated from

235 mid-August to mid-September to the winter velocities and then accelerated again by 0.5 m d^{-1} at Concordia in mid-September.

The first and second snowmelt event occurred in the same period as the spring speed-up and lake evolution. Hence, it seems that the first melt events had a large influence on the spring speed-up. Possibly the surface melt water could initiate lake formation, though, it could not be proven due to the low spatial resolution of the remote sensing data. The temporal comparison of the supraglacial lakes and surface velocity showed that the beginning of lake formation and spring speed-up occurred in the

240 same time leading to the assumption that the lake drainage hardly influence on the surface velocity. In 2018 to 2020, the lake drainage started in the period around the summer velocity peak and coincided with a velocity decrease. Though, in 2017 and 2021, lake drainage started shortly before the fall speed-up and in 2022, between spring speed-up and summer peak.

The pattern and peak of the runoff-index changed every year: 2017 was characterized with a slow increase during May and June with two distinctive peaks in mid-July (21 July) and early-August (5 August); 2018 by a steady and slow rise with lows

245 and highs (12 June, 22 July, 10 August); 2019 by a significant increase begin of July, a constant run-off until end of July, and a subsequent peak in early August; 2020 by a slow gain from May until August and two peaks (3 and 25 August) with continuous runoff-index between both dates; 2021 by a continuous increase until end of July succeeded by a high (28 July); 2022 by a continuous low runoff-index until end of June and a sudden rise leading to three distinct peaks (8 July, 26 July, 19 August).

4.2 Spatial relationship

250 The spatial relationship of supraglacial lakes, snowmelt, and surface velocity for the two periods of spring speed-up (13 April-07 May) and summer peak (07 May-18 July) is presented as an example for 2018 in Figure 3. This year was chosen because the events were clearly recognizable. In the first period (Fig. 3a), the surface velocity between Urdukas and Gore ranged from 0.2-0.4 m d^{-1} and between Gore and Concordia from 0.4-0.6 m d^{-1}. During this time, the main branch between Gore and Concordia and the neighboring tributary glaciers up to 4700 m a.s.l. exhibited snowmelt covering an area of 237 km^2. The

255 supraglacial lakes were mostly located between glacier tongue and Gore. In the second period (Fig. 3b), the higher velocities of 0.4-0.6 m d^{-1} expanded downwards to the confluence of Mandu Glacier and the snowmelt upwards to 5600 m a.s.l. covering an area of 327 km^2. Both figures show the large areas already affected by snowmelt at the beginning of May and the comparatively small area of the supraglacial lakes.
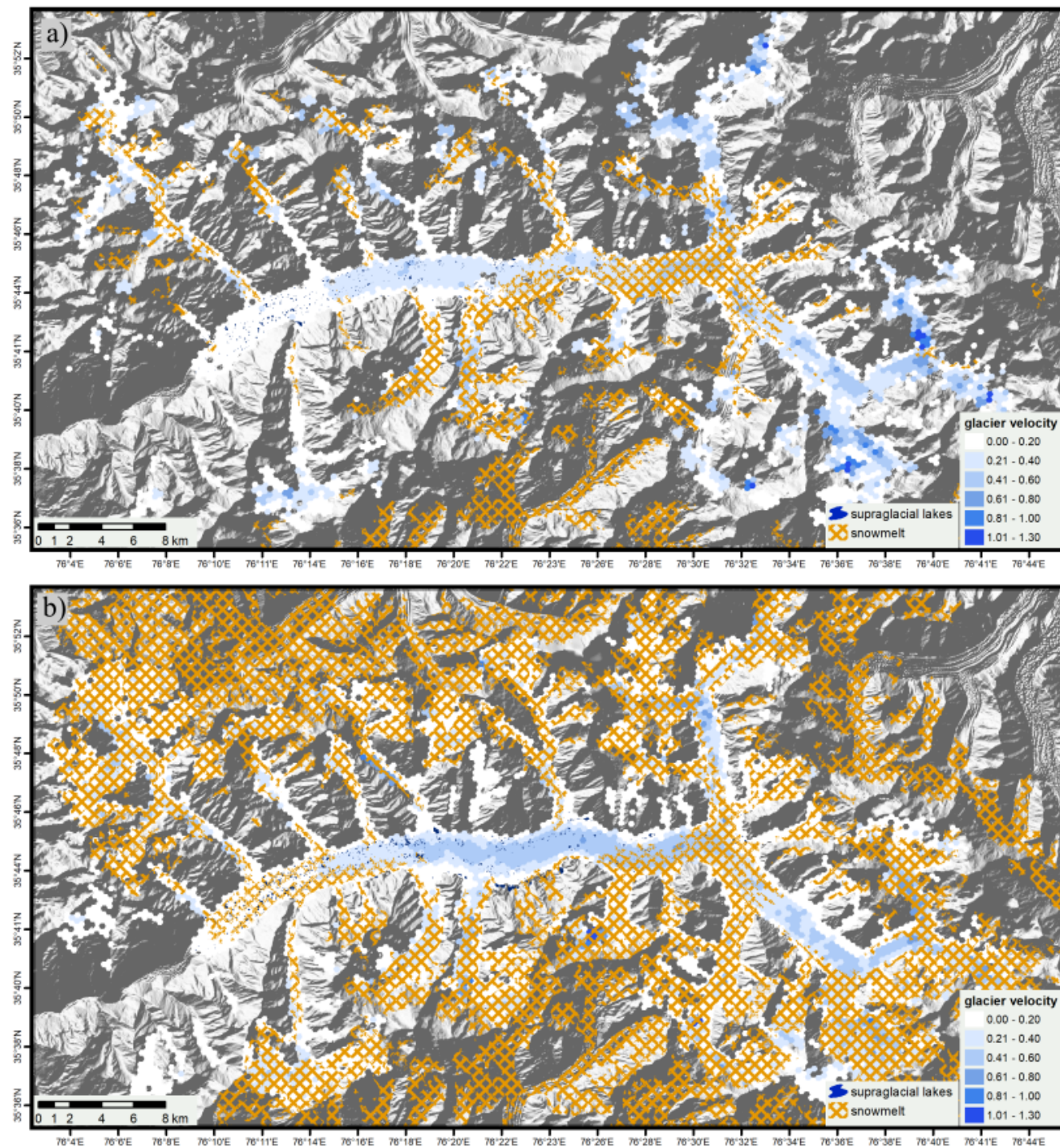
Figure 3. Spatial relationship of the aggregated supraglacial lake area, aggregated snowmelt, and median surface velocity from 13 April to 7 May 2018 (a) and 7 May to 18 July 2018 (b)

4.3 Pearson Correlation

260 Figure 4 lists the Pearson correlation of all variables for the first period defined from the first day with positive air temperatures to the maximum glacier velocity and the second period defined from the maximum glacier velocity until the end of the ablation season. Correlation results can be found in the supplementary materials (Table A1 and A2)). The temperature had a strong relationship with snowmelt (0.70–0.90 in first period, 0.71–0.95 in second period) as well as with supraglacial lakes (0.58–0.87 in first period, 0.68–0.89 in second period) and a low correlation with supraglacial lakes (0.39) in the second period in 2020. The

265 period between July and September 2020 was cloudier than usual which could indicate a stronger Indian Summer Monsoon and hence a higher precipitation resulting in short-term lake fluctuations. In the first period of 2018 and 2019, snowmelt and velocity up-glacier of Gore showed a high correlation (0.63–0.77 and 0.60–0.92), in the first period of 2020 and 2022 already upwards of Yermanendu (0.68–0.93 and 0.81–0.95, respectively) and in 2017 and 2021 upwards of Urdukas (0.92-0.94, 0.73–0.89). In the second period, only in 2017, 2019 and 2020, a high correlation upwards Gore (0.6-0.80) and Concordia

270 (0.64), respectively, existed. Though, in the second period in 2018 and 2021, the correlations were negative. In the first periods from 2017 to 2022, the pattern of snowmelt and velocity was similar to that of supraglacial lakes and velocity with lower correlations at Urdukas with an increase till Concordia. In the first period, lakes and the velocity had a significant positive correlation downglacier of Yermanendu in 2017 (0.86-0.91), up-glacier of Gore in 2018 (0.63-0.69), in 2019 (0.77-0.96), and 2020 (0.73-0.96) and upwards of Yermanendu in 2021 (0.82-0.98) and 2022 (0.74-0.86). Though, in the second period, a

275 positive correlation existed upwards of Gore in 2017 (0.63-0.69), in 2019 (0.68-0.87), in 2020 (0.73-0.96), and 2022 (0.56-0.73). The remaining correlations were not significant. Precipitation and velocity showed no significant correlation. A high degree of correlation existed between snowmelt and runoff-index (0.65–0.93) respectively supraglacial lakes (0.63–0.94) except in the second period in 2019 (0.51) and 2020 (-0.11). In the first period, the relationship between runoff-index and velocity had the same pattern as snowmelt and velocity: in 2017, 2018, and 2019, strong relationships existed upglacier of Gore, in 2020

280 and 2022 upwards of Yermanendu, and in 2021 upwards of Urdukas. In the second period a strong relationship for runoff-index and velocity at Yermanendu and Gore (0.64–0.79) was observed only in the 2019 dataset.

4.4 Linear Regression

Table 2 and 3 list the results of the linear regression with R^2 and the regression coefficient. In 2018, 2020, and 2022, temperature and snowmelt respectively supraglacial lakes have a high R^2 (0.65-0.83), but the dependency is low (0-7 °C/km^2). Snowmelt

285 and surface velocity have a high R^2 for the first period in 2017 on the area up-glacier of Urdukas (0.85-0.88), 2019 at Concordia (0.84), in 2020 (0.78-0.87) and 2022 (0.74-0.9) up-glacier of Gore, and in 2021 (0.7-0.8) up-glacier of Yermanendu. The regression coefficient lies at 832-1897 km^{2}d/m. The second period shows a low R^2. Supraglacial lakes and surface velocity shows a high correlation up-glacier of Urdukas in the first period of 2017 (0.73-0.87), up-glacier of Gore in the first period of 2021 (0.71-0.94) and at Concordia in the first period of 2018 (0.86), 2019 (0.92), 2020 (0.91), and 2022 (0.75) and in the

290 second period of 2019 (0.75). Though, the dependency of supraglacial lakes to velocity is minimal (4-11 km^{2}d/m). R^2 and dependency of precipitation to surface velocity is not significant. Snowmelt and runoff-index as well as supraglacial lakes and
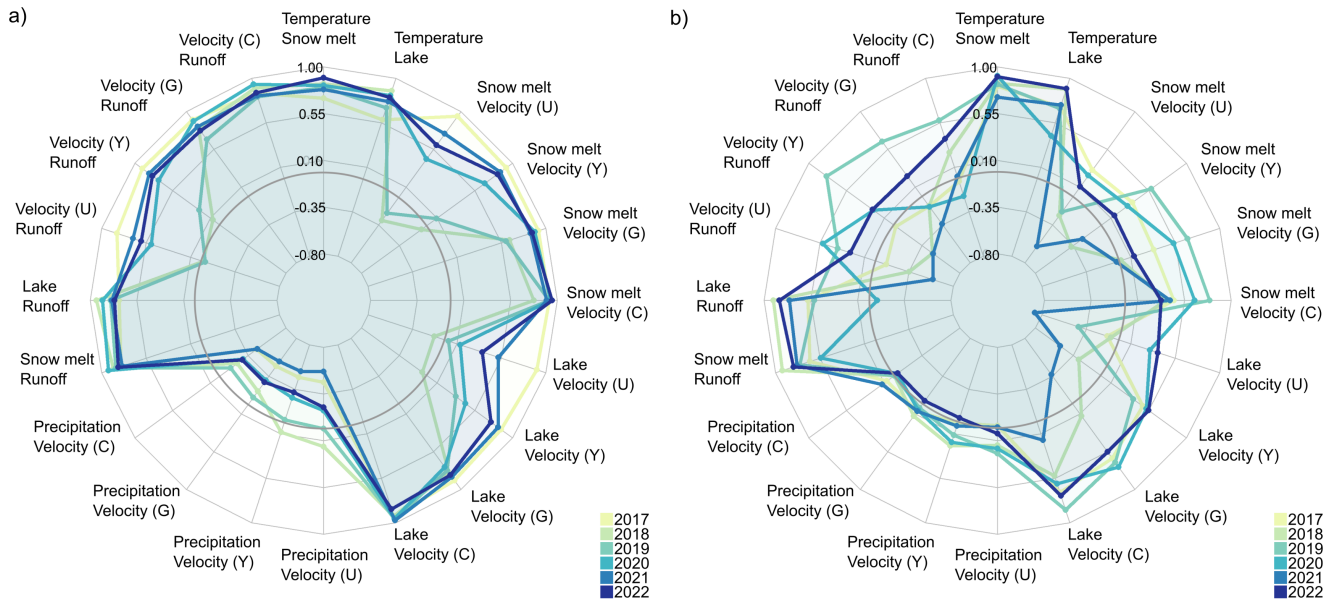
Figure 4. Pearson correlation of glacier and climate variables for first period defined from the first day with positive air temperatures to the maximum glacier velocity (a) and second period defined from the maximum glacier velocity until the end of the ablation season (b). The null line is displayed in grey. The abbreviation U stands for Urdukas, Y for Yermanendu, G for Gore, and C for Concordia.

runoff-index show the pattern with similar R^2 (0.77-0.88), however the dependency of snowmelt (171-370 km^2/km^2) is larger than the one of supraglacial lakes (1-4 km^2/km^2). The dependency of the surface velocity to runoff-index is not significant (0 m/d km^2).

4.5   Temporal delay between snowmelt and velocity

Following the high correlation of snowmelt area and surface velocity during the spring period almost every year and the process-oriented relation between melt onset, inefficient drainage and basal sliding, we investigated the temporal delay between snowmelt and velocity. In particular, we analyzed the time lag in days between the first seasonal snowmelt peak and the first relative velocity maximum at Urdukas, Yermanendu, Gore, and Concordia. The temporal lag between the two parameters is generally longest at Concordia (34 $\pm$ 25 days), followed downglacier by Gore (12 $\pm$ 19 days) and Yermanendu (12 $\pm$14 days), and shortest at Urdukas (10 $\pm$ 16 days). Given the period from 2017 to 2022 there is an indication that the temporal delay between the first seasonal snowmelt peak and the first relative velocity maximum is decreasing.

5   Discussion

In the last chapter, we explain how basal sliding and hydrological drainage occurred and the impact of snowmelt and supraglacial lakes on this process.

Table 2. Linear regression given as R^2 and the regression coefficient (in parentheses) of all variables for 2017-2019. Only significant trends according to a 95 % confidence interval based on the Mann–Kendall test are shown. Results with an R^2 smaller than 0.3 are displayed in red and those larger than 0.7 are displayed in green.

	Period I 2017 21.03.-04.06.	Period II 2017 05.06.-30.09.	Period I 2018 12.03.-17.07.	Period II 2018 18.07.-30.09.	Period I 2019 27.03.-12.07.	Period II 2019 13.07.–30.09.
Temperature – Snowmelt (°C/km²)	0.48 (0)	0.65 (0)	0.7 (0)	0.7 (0)	0.64 (0)	0.68 (0)
Temperature – Supraglacial Lake (°C/km²)	0.32 (5)	0.5 (7)	0.76 (5)	0.78 (7)	0.49 (3)	0.47 (9)
Snowmelt – Velocity at Urdukas (km²d/m)	0.88 (1897)	0.08 (455)			0.03 (-557)	
Snowmelt – Velocity at Yermanendu (km²d/m)	0.84 (1161)	0.11 (511)		0.12 (-598)	0.0 (153)	0.32 (742)
Snowmelt – Velocity at Gore (km²d/m)	0.85 (889)	0.10 (235)	0.39 (1053)		0.34 (754)	0.44 (707)
Snowmelt – Velocity at Concordia (km²d/m)	0.85 (970)	0.19 (225)	0.59 (1061)	0.12 (374)	0.84 (1007)	0.62 (783)
Supraglacial Lake – Velocity at Urdukas (km²d/m)	0.82 (8)		0.00 (-4)		0.0 (0)	
Supraglacial Lake – Velocity at Yermanendu (km²d/m)	0.73 (5)	0.22 (4)			0.0 (5)	
Supraglacial Lake – Velocity at Gore (km²d/m)	0.79 (4)	0.39 (3)	0.63 (11)		0.59 (10)	0.45 (3)
Supraglacial Lake – Velocity at Concordia (km²d/m)	0.87 (4)	0.47 (2)	0.86 (11)	0.26 (5)	0.92 (11)	0.75 (4)
Precipitation – Velocity at Urdukas (mm d/m)	0.20 (-131)	0.0 (-8)				
Precipitation – Velocity at Yermanendu (mm d/m)	0.21 (-84)					
Precipitation – Velocity at Gore (mm d/m)	0.21 (-63)	0.0 (5)	0.02 (-31)		0.0 (-20)	
Precipitation – Velocity at Concordia (mm d/m)	0.19 (-67)	0.0 (4)	0.04 (-33)		0.01 (-26)	-0.01 (-1)
Snowmelt - Runoff-Index (km²/km²)	0.64 (411)	0.41 (66)	0.77 (295)	0.86 (171)	0.73 (370)	0.56 (141)
Supraglacial Lake - Runoff-Index (km²/km²)	0.51 (2)	0.32 (0)	0.87 (3)	0.82 (1)	0.64 (4)	0.25 (0)
Velocity at Urdukas - Runoff-Index (m/d km²)	0.71 (0)	0.00 (0)				0.13 (0)
Velocity at Yermanendu - Runoff-Index (m/d km²)	0.82 (0)	0.0 (0)		0.21 (0)	0.04 (0)	0.61 (0)
Velocity at Gore - Runoff-Index (m/d km²)	0.80 (0)		0.64 (0)	0 (0.0)	0.43 (0)	0 (0.4)
Velocity at Concordia - Runoff-Index (m/d km²)	0.71 (0)		0.80 (0)		0.65 (0)	0.32 (0)

5.1 Transition between efficient and inefficient drainage

Although each year is different, we are following only a generalised description of the process. The transition of winter to spring was typically observed between the end of March and the end of April, as positive temperatures begin to persist above 0°C for periods of multiple days up to 4700 m a.s.l. (Copland, 2011). The snow on the main branch usually has already melted to Gore at this time. This warm period causes supraglacial lake formation up to 4300 m a.s.l. due to meltwater from snow and ice and the first snowmelt on the tributary glaciers and main branch up to 4700 m a.s.l. The surface meltwater flows into the ice via crevasses and reaches the cavities at the glacier bed via vertical conduits. As the drainage system is inefficient, the channels cannot cope with the influx of the first snowmelt causing a high subglacial water pressure and separation of ice from the bed with a subsequent basal motion (Mair et al., 2001; Macgregor et al., 2005; Burgess et al., 2013; Nanni et al., 2023). The high correlation between snowmelt and velocity confirms this phenomenon. The spring speed-up with an increase of 0.1-0.15 m d⁻¹ affects the complete glacier area between Urdukas and Concordia. In the years 2017, 2019, 2020, and 2021, the velocity at

Table 3. Linear regression given as R^2 and the regression coefficient (in parentheses) of all variables for 2020-2022. Only significant trends according to a 95 % confidence interval based on the Mann–Kendall test are shown. Results with an R^2 smaller than 0.3 are displayed in red and those larger than 0.7 are displayed in green.

	Period I 2020 21.03.-24.06.	Period II 2020 25.06.-30.09.	Period I 2021 07.03.-19.06.	Period II 2021 20.06.-30.09.	Period I 2022 05.03.-08.07.	Period II 2022 09.07.–30.09.
Temperature – Snowmelt (°C/km²)	0.67 (0)	0.83 (0)	0.61 (0)	0.5 (0)	0.80 (0)	0.81 (0)
Temperature – Supraglacial Lake (°C/km²)	0.68 (5)		0.58 (7)	0.66 (9)	0.67 (4)	0.79 (7)
Snowmelt – Velocity at Urdukas (km²d/m)	0.18 (936)		0.53 (2946)	0.36 (-1085)	0.35 (5149)	0.0 (246)
Snowmelt – Velocity at Yermanendu (km²d/m)	0.44 (700)		0.72 (1358)	0.05 (-348)	0.66 (3100)	
Snowmelt – Velocity at Gore (km²d/m)	0.78 (831)	0.28 (839)	0.70 (1164)		0.74 (1215)	
Snowmelt – Velocity at Concordia (km²d/m)	0.87 (972)	0.41 (588)	0.80 (1059)	0.16 (253)	0.90 (1031)	
Supraglacial Lake – Velocity at Urdukas (km²d/m)	0.0 (3)	0.07 (1)	0.25 (11)	0.53 (-8)		0.14 (9)
Supraglacial Lake – Velocity at Yermanendu (km²d/m)	0.18 (5)	0.26 (3)	0.67 (7)	0.07 (-3)	0.54 (27)	0.30 (6)
Supraglacial Lake – Velocity at Gore(km²d/m)	0.52 (7)	0.53 (3)	0.71 (6)	0.0 (0)	0.6 (12)	0.30 (4)
Supraglacial Lake – Velocity at Concordia (km²d/m)	0.91 (10)	0.36 (1)	0.94 (6)		0.75 (9)	0.53 (4)
Precipitation – Velocity at Urdukas (mm d/m)			0.31 (-255)		0.04 (-137)	
Precipitation – Velocity at Yermanendu (mm d/m)	0.06 (-28)	0.02 (49)	0.27 (-96)		0.09 (-87)	
Precipitation – Velocity at Gore (mm d/m)	0.08 (-28)		0.26 (-81)		0.06 (-28)	
Precipitation – Velocity at Concordia (mm d/m)	0.07 (-30)		0.20 (-61)		0.07 (-22)	
Snowmelt - Runoff-Index (km²/km²)	0.88 (367)	0.28 (160)	0.62 (465)	0.60 (129)	0.69 (277)	0.62 (123)
Supraglacial Lake - Runoff-Index (km²/km²)	0.77 (4)		0.62 (2)	0.48 (1)	0.59 (2)	0.55 (1)
Velocity at Urdukas - Runoff-Index (m/d km²)		0.26 (0)	0.46 (0)	0.35 (0)	0.35 (0)	
Velocity at Yermanendu - Runoff-Index (m/d km²)	0.51 (0)	0.04 (0)	0.68 (0)	0.22 (0)	0.62 (0)	
Velocity at Gore - Runoff-Index (m/d km²)	0.78 (0)	0.0 (0)	0.66 (0)	0 (0.1)	0.59 (0)	
Velocity at Concordia - Runoff-Index (m/d km²)	0.88 (0)	0.02 (0)	0.67 (0)		0.72 (0)	

Gore exceeds that at Concordia suggesting that basal sliding is greatest at this location. The persisting warm temperatures cause the lake creation and expansion as well as the continued snowmelt. With the rise in temperatures, the snowmelt expands up to 5600 m a.s.l and provides a continuous water influx into the channels and continuous velocity increase to up to 0.59 m d^{-1}

320 from June to July. The water pressure and the resulting frictional heat leading to a melting of the ice walls causes an expansion of the channels and thus, leads to a transition from an inefficient to an efficient drainage (Schoff, 2010; Sundal et al., 2011; Benn et al., 2017). The increase in the capacity of the drainage system reduces the water pressure and slows the glacier motion between Urdukas and Concordia down to the winter values (0.25-0.39 m d^{-1}) (Nienow et al., 1998; Hewitt, 2013; Vincent and Moreau, 2016). Afterwards, an increase in the time delayed runoff at the glacier terminus is observable. Only early July 2022,

325 an abrupt change from low to high runoff is recognizable indicating a faster transition to an efficient drainage. In the other years, however, the runoff is linearly increasing or fluctuating gradually through time between minimum and maximum extent. Presumably, the higher summer velocities provokes the creation of crevasses and cracks and thus enables the drainage of the

supraglacial lakes. The drained lake which is only disposable after the slowdown lead, in addition to the snowmelt, to a water surplus and hence to an increase in water pressure and basal sliding during fall, but with lower magnitude by 0.1-0.2 m d^{-1} than the summer velocity peak (Hewitt, 2013; Hart et al., 2022; Nanni et al., 2023).

330

In summary, we have found that 1) higher temperature lead to a rise in lake onset and snowmelt equally, 2) the snowmelt water causes the spring speed-up and the high summer glacier velocities, 3) the drained supraglacial lake and meltwater provokes the fall speed-up, 4) in the first half of the ablation (till to the peak of the supraglacial lakes) the runoff is mostly fed by the snowmelt, and in the second half, as well by the supraglacial lakes, but with a smaller amount, and 5) a higher number

335 and area of lakes are an indicator of higher temperatures as it was observed during the spring heat wave in 2022 (Otto et al., 2023). Although the main branch of Baltoro Glacier is thermally insulated due to its debris coverage (larger than the critical thickness), the debris-free tributary glaciers are affected by higher temperatures and melting provoking change in ice dynamics.

5.2 Impact of snowmelt and supraglacial lakes

The snowmelt covers the largest area of 319-353 km^2 in mid-July to mid-August. Assuming a snow depth of 1-1.5 m and the

340 density for settled snow of 350 kg m^{-3} at the end of the ablation season Mayer et al. (2014), this could roughly estimated to a snow water equivalent of 122-188 million m^3. However, the supraglacial lakes cover a total annual area of 3.6-5.9 km^2 and a maximal volume of 60 millions m^3 assuming an average water depth of 10 m (Liu et al., 2015). The retrieval of snow water equivalent over flat terrain using passive microwave satellite data with a spatial resolution of 25 km has been demonstrated to be achievable (Derksen et al., 2002; Walker and Silis, 2002). However, this approach is not suitable for our study area, but

345 further investigations are ongoing regarding the applicability of high-resolution imagery (Tsang et al., 2022). Consequently, the present study exclusively relied on snowmelt area.

In Wendleder et al. (2018), we inferred that warmer spring seasons (April-May) with higher precipitation or melt rates would lead to increased formation of supraglacial lakes and that the discharge of the supraglacial lakes would cause an increased basal sliding. Increased availability of Earth Observation data since 2016 has now enabled a continuous mapping of the seasonal

350 evolution of supraglacial lakes (Wendleder et al., 2021a) and snowmelt and thus provides an insight into the detailed process. The observation that higher temperatures during the early melt season provokes a rise in number and area of supraglacial lakes and surface velocities is confirmed in this study.

6 Conclusions

To better understand the process whether and how the discharge water of the supraglacial lakes triggers the basal sliding, we

355 combined the glaciological variables, namely surface velocity, extent of supraglacial lakes, snowmelt, and runoff-index derived from Earth Observation data, and the climate variables, namely air temperature and precipitation from the HAR data set, in a spatio-temporal analysis. The multi-parameter time series were analysed by the Pearson correlation and linear regression. Our study shows that the snowmelt of the tributary glaciers, covering up to 64 % of the total area of Baltoro Glacier and lasting from April to November/December, has the greatest impact to the basal sliding that leads to the spring speed-up and the summer

360 velocity peak and thus to the transition from inefficient and efficient drainage. The discharge from snowmelt accounts for the largest amount of runoff. The supraglacial lakes with a cumulative area of 3.6-5.9 km^2 contribute to the fall speed-up which has a lower magnitude by 0.1-0.2 m d^{-1} than the summer velocity peak. Snowmelt as well as supraglacial lakes are affected by positive temperatures. Both are initialised by the abrupt transition from winter to spring characterized by a period of several days with positive temperatures from the end of March to the end of April and influenced by continued, high temperatures

365 during the ablation period. The year 2022 exhibits notable climatic impacts in the form of a sustained warm period, giving rise to a series of consequential phenomena. This includes an increasing number of supraglacial lakes, an advancement in the timing of maximal lake area, and a substantial amplification of snowmelt. These factors collectively provoke heightened surface velocities during spring, summer, and autumn, driven predominantly by the mechanism of basal sliding. Additionally, this altered dynamic triggers a more rapid transition towards a efficient drainage system. There exists an indication that the

370 temporal delay between initial peak of seasonal snowmelt and first relative velocity maximum is decreasing. This observation warrants a careful interpretation, suggesting that the glacier's response is intensifying in relation to the processes of snowmelt and velocity. Consequently, this increases the glacier's potential for stronger responsiveness to climatic variations, in particular elevated temperatures, thereby implying an augmented susceptibility to the effects of climate change. Furthermore, a faster transition to an efficient drainage has a less storage efficiency during extreme events and thus a higher risk of flood hazards.

375 *Code and data availability.* The code is available on request. The TerraSAR-X data are available through the DLR (©DLR 2019-2022), Sentinel-1 and 2 data are provided by the DLR Processing and Archiving Center (PAC) / Long-Term Archive (LTA) (©ESA 2019-2022), PlanetScope data are available through Planet (©Planet 2019-2022), and the High Asia Refined analysis (HAR) dataset by the Chair of Climatology, TU Berlin.

Author contributions. AW, AS, DJQ, CM, and MB designed the research. AW analyzed the data and results and wrote the manuscript. JB
380 helped with the spatial representation, JI calculated the surface velocity fields, TE determined the temporal delay, and PD processed the MAJA corrected Sentinel-2 data. All authors helped to edit and to improve the manuscript.

Competing interests. The authors declare that they have no competing interests

References

Armstrong, W. H., Anderson, R. S., and Fahnestock, M. A.: Spatial Patterns of Summer Speedup on South Central Alaska Glaciers, Geophysical Research Letters, 44, 9379–9388, https://doi.org/10.1002/2017GL074370, 2017.

Bartholomaus, T., Anderson, R., and Anderson, S.: Response of glacier basal motion to transient water storage., Nature Geosci, 1, 33–37, https://doi.org/10.1038/ngeo.2007.52, 2008.

Benn, D., Thompson, S., Gulley, J., Mertes, J., Luckman, A., and Nicholson, L.: Structure and evolution of the drainage system of a Himalayan debris-covered glacier, and its relationship with patterns of mass loss, The Cryosphere, 11, 2247–2264, https://doi.org/10.5194/tc-11-2247-2017, 2017.

Benn, D. I., Fowler, A. C., Hewitt, I., and Sevestre, H.: A general theory of glacier surges, Journal of Glaciology, 65, 701–716, https://doi.org/10.1017/jog.2019.62, 2019.

Berthier, E. and Brun, F.: Karakoram geodetic glacier mass balances between 2008 and 2016: persistence of the anomaly and influence of a large rock avalanche on Siachen Glacier, Journal of Glaciology, 65, 494–507, https://doi.org/10.1017/jog.2019.32, 2019.

Bookhagen, B. and Burbank, D.: Topography, relief and TRMM-derived rainfall variations along the Himalaya, 33, https://doi.org/10.1029/2006GL026037, 2006.

Boulton, G. S. and Hindmarsh, R. C. A.: Sediment deformation beneath glaciers: Rheology and geological consequences, Journal of Geophysical Research: Solid Earth, 92, 9059–9082, https://doi.org/10.1029/JB092iB09p09059, 1987.

Brun, F., Wagnon, P., Berthier, E., Shea, J., Immerzeel, W., Kraaijenbrink, P., Vincent, C., Reverchon, C., Shrestha, D., and Arnaud, Y.: Ice cliff contribution to the tongue-wide ablation of Changri Nup Glacier, Nepal, central Himalaya, The Cryosphere, 12, 3439–3457, https://doi.org/10.5194/tc-12-3439-2018, 2018.

Burgess, E., Forster, R., and Larsen, C.: Flow velocities of Alaskan glaciers, Nat Commun, 4, 9059–9082, https://doi.org/10.1038/ncomms3146, 2013.

Buri, P., Miles, E., Steiner, J., Ragettli, S., and Pellicciotti, F.: Supraglacial Ice Cliffs Can Substantially Increase the Mass Loss of Debris-Covered Glaciers, Geophysical Research Letters, 48, 1–11, https://doi.org/10.1029/2020gl092150, 2021.

Copland, L.: Melting Processes, pp. 733–735, https://doi.org/10.1007/978-90-481-2642-2_350, 2011.

Copland, L., Sharp, M. J., and Nienow, P. W.: Links between short-term velocity variations and the subglacial hydrology of a predominantly cold polythermal glacier, Journal of Glaciology, 49, 337–348, https://doi.org/10.3189/172756503781830656, 2003.

Cuffey, K. and Paterson, W.: The physics of glaciers. Fourth edition, p. 704pp, 2010.

Derksen, C., Walker, A., LeDrew, E., and Goodison, B.: Time-series analysis of passive-microwave-derived central North American snow water equivalent imagery, Annals of Glaciology, 34, 1–7, https://doi.org/10.3189/172756402781817815, 2002.

Dobreva, I. D., Bishop, M. P., and Bush, A. B. G.: Climate–Glacier Dynamics and Topographic Forcing in the Karakoram Himalaya: Concepts, Issues and Research Directions, Water, 9, 1–29, https://doi.org/10.3390/w9060405, 2017.

ESA: COPERNICUS Digital Elevation Model (DEM), https://doi.org/10.5270/ESA-c5d3d65, 2019.

Evatt, G. W., Mayer, C., Mallinson, A., Abrahams, I. D., Heil, M., and Nicholson, L.: The secret life of ice sails, Journal of Glaciology, 63, 1049–1062, https://doi.org/10.1017/jog.2017.72, 2017.

Flowers, G. E.: Modelling water flow under glaciers and ice sheets, Proc. R. Soc. A., 471, 1347–1365, https://doi.org/10.1098/rspa.2014.0907, 2015.

Friedl, P., Seehaus, T. C., Wendt, A., Braun, M. H., and Höppner, K.: Recent dynamic changes on Fleming Glacier after the disintegration of Wordie Ice Shelf, Antarctic Peninsula, The Cryosphere, 12, 1–41, https://doi.org/10.5194/tc-2017-91, 2018.

Friedl, P., Seehaus, T., and Braun, M. H.: Global time series and temporal mosaics of glacier surface velocities derived from Sentinel-1 data, Earth System Science Data, 13, 4653–4675, https://doi.org/10.5194/essd-13-4653-2021, 2021.

Glasser, N.: 8.6 Water in Glaciers and Ice Sheets, pp. 61–73, https://doi.org/10.1016/B978-0-12-374739-6.00195-0, 2013.

Hagolle, O., Huc, M., Desjardins, C., Auer, S., and Richter, R.: MAJA Algorithm Theoretical Basis Document, Stochastic Environmental Research and Risk Assessment, Version 1.0, https://doi.org/10.5281/zenodo.1209633, 2017.

Hart, J., Young, D., Baurley, N., Robson, B. A., and Martinez, K.: The seasonal evolution of subglacial drainage pathways beneath a soft-bedded glacier, Commun Earth Environ, 3, https://doi.org/10.1038/s43247-022-00484-9, 2022.

Hausdorff, F.: Grundzüge der Mengenlehre, Veit, Leipzig, 1914.

Hewitt, I.: Seasonal changes in ice sheet motion due to melt water lubrication, Earth and Planetary Science Letters, 371-372, 16–25, https://doi.org/10.1016/j.epsl.2013.04.022, 2013.

Hoffman, M., Andrews, L., Price, S., Catania, G. A., Neumann, T. A., Lüthi, M. P., Gulley, J., Ryser, C., Hawley, R. L., and Morriss, B.: Greenland subglacial drainage evolution regulated by weakly connected regions of the bed, Nature Communications, 7, https://doi.org/10.1038/ncomms13903, 2016.

Iken, A. and Bindschadler, R. A.: Combined measurements of Subglacial Water Pressure and Surface Velocity of Findelengletscher, Switzerland: Conclusions about Drainage System and Sliding Mechanism, Journal of Glaciology, 32, 101–119, https://doi.org/10.3189/S0022143000006936, 1986.

Jiskoot, H.: Dynamics of Glaciers, Encyclopedia of snow, ice and glaciers, V.P. Singh, P. Singh, and U.K. Haritashya, Editors. 2011, pp. 245–256, 2011.

Liu, Q., Christoph, M., and Shiyin, L.: Distribution and interannual variability of supraglacial lakes on debris-covered glaciers in the Khan Tengri-Tumor Mountains, Central Asia, Environmental Research Letters, 10, 014 014, https://doi.org/10.1088/1748-9326/10/1/014014, 2015.

Lliboutry, L.: General Theory of Subglacial Cavitation and Sliding of Temperate Glaciers, Journal of Glaciology, 7, 21–58, https://doi.org/10.3189/S0022143000020396, 1968.

Macgregor, K. R., Riihimaki, C. A., and Anderson, R. S.: Spatial and temporal evolution of rapid basal sliding on Bench Glacier, Alaska, USA, Journal of Glaciology, 51, 49–63, https://doi.org/10.3189/172756505781829485, 2005.

Mair, D., Nienow, P., Willis, I., and Sharp, M.: Spatial patterns of glacier motion during a high-velocity event: Haut Glacier d'Arolla, Switzerland, Journal of Glaciology, 47, 9–20, https://doi.org/10.3189/172756501781832412, 2001.

Mayer, C., Lambrecht, A., Belo, M., Smiraglia, C., and Diolaiutt, G.: Glaciological characteristics of the ablation zone of Baltoro glacier, Karakoram, Pakistan, Annals of Glaciology, 43, 123–131, 2006.

Mayer, C., Lambrecht, A., Oerter, H., Schwikowski, M., Vuillermoz, E., Frank, N., and Diolaiuti, G.: Accumulation Studies at a High Elevation Glacier Site in Central Karakoram, Advances in Meteorology, 2014, 1–12, https://doi.org/10.1155/2014/215162, 2014.

Miles, K. E., Hubbard, B., Irvine-Fynn, T. D. L., Miles, E. S., Quincey, D. J., and Rowan, A. V.: Hydrology of debris-covered glaciers in High Mountain Asia, Earth-Science Reviews, 207, 103 212, https://doi.org/10.1016/j.earscirev.2020.103212, 2020.

Nagler, T. and Rott, H.: Retrieval of wet snow by means of multitemporal SAR data, IEEE Transactions on Geoscience and Remote Sensing, 38, 754–765, https://doi.org/10.1109/36.842004, 2000.

Nanni, U., Scherler, D., Ayoub, F., Millan, R., Herman, F., and Avouac, J.-P.: Climatic control on seasonal variations in mountain glacier surface velocity, The Cryosphere, 17, 1567–1583, https://doi.org/10.5194/tc-17-1567-2023, 2023.

Nicholson, L. and Benn, D.: Calculating ice melt beneath a de-bris layer using meteorological data, Journal of Glaciology, 52, 463–470, https://doi.org/10.3189/172756506781828584, 2006.

460 Nienow, P., Sharp, M., and Willis, I.: Seasonal changes in the morphology of the subglacial drainage system, Haut Glacier d'Arolla, Switzerland, Earth Surface Processes and Landforms, 23, 825–843, 1998.

Nolan, M. and Echelmeyer, K.: Seismic detection of transient changes beneath Black Rapids Glacier, Alaska, U.S.A.: II. Basal morphology and processes, Journal of Glaciology, 45, 132–146, https://doi.org/10.3189/S0022143000003117, 1999.

Obilor, E. I. and Amadi, E.: Test for Significance of Pearson's Correlation Coefficient (r), International Journal of Innovative Mathematics,
465 Statistics and Energy Policies, 6, 11–23, 2018.

Otto, F. E. L., Zachariah, M., Saeed, F., Siddiqi, A., Kamil, S., Mushtaq, H., Arulalan, T., AchutaRao, K., Chaithra, S. T., Barnes, C., Philip, S., Kew, S., Vautard, R., Koren, G., Pinto, I., Wolski, P., Vahlberg, M., Singh, R., Arrighi, J., van Aalst, M., Thalheimer, L., Raju, E., Li, S., Yang, W., Harrington, L. J., and Clarke, B.: Climate change increased extreme monsoon rainfall, flooding highly vulnerable communities in Pakistan, Environmental Research: Climate, 2, 025 001, https://doi.org/10.1088/2752-5295/acbfd5, 2023.

470 Quincey, D. J., Copland, L., Mayer, C., Bishop, M., Luckman, A., and Belò, M.: Ice velocity and climate variations for Baltoro Glacier, Pakistan, Journal of Glaciology, 55, 1061–1071, https://doi.org/https://doi.org/10.3189/002214309790794913, 2009.

Rada Giacaman, C. A. and Schoof, C.: Channelized, distributed, and disconnected: spatial structure and temporal evolution of the subglacial drainage under a valley glacier in the Yukon, The Cryosphere, 17, 761–787, https://doi.org/10.5194/tc-17-761-2023, 2023.

Rott, H. and Mätzler, C.: Possibilities and Limits of Synthetic Aperture Radar for Snow and Glacier Surveying, Annals of Glaciology, 9,
475 195–199, https://doi.org/10.3189/S0260305500000604, 1987.

Röthlisberger, H.: Water Pressure in Intra- and Subglacial Channels, Journal of Glaciology, 11, 177–203, https://doi.org/10.3189/S0022143000022188, 1972.

Sakai, A.: Glacial lakes in the Himalayas: a review on formation and expansion processes, Global Environmental Research, pp. 23–30, 2012.

Sakai, A. and Fujita, K.: Formation conditions of supraglacial lakes on debris covered glaciers in the Himalaya, Journal of Glaciology, 56,
480 177–181, https://doi.org/10.3189/002214310791190785, 2006.

Scher, C., Steiner, N. C., and McDonald, K. C.: Mapping seasonal glacier melt across the Hindu Kush Himalaya with time series synthetic aperture radar (SAR), The Cryosphere, 15, 4465 – 4482, https://doi.org/10.5194/tc-15-4465-2021, 2021.

Schmitt, A., Wendleder, A., and Hinz, S.: The Kennaugh element framework for multi-scale, multi-polarized,multi-temporal and multi-frequency SAR image preparation, ISPRS Journal of Photogrammetry and Remote Sensing, 102, 122–139, https://doi.org/10.1016/S0031-
485 3203(00)00136-9, 2015.

Schmitt, A., Wendleder, A., Kleynmans, R., Hell, M., Roth, A., and Hinz, S.: Multi-Source and Multi-Temporal Image Fusion on Hypercomplex Bases, Remote Sensing, 12, 2083–2096, https://doi.org/10.3390/rs12060943, 2020.

Schoff, C.: Ice-sheet acceleration driven by melt supply variability, Nature, 468, 803–806, https://doi.org/10.1038/nature09618, 2010.

Shi, J. and Dozier, J.: Inferring snow wetness using C-band data from SIR-C's polarimetric synthetic aperture radar, IEEE Transactions on
490 Geoscience and Remote Sensing, 33, 905–914, https://doi.org/10.1109/36.406676, 1995.

Strozzi, T., Luckman, A., Murray, T., Wegmuller, U., and Werner, C. L.: Glacier motion estimation using SAR offset-tracking procedures, IEEE Transactions on Geoscience and Remote Sensing, 40, 2384–2391, https://doi.org/10.1109/TGRS.2002.805079, 2002.

Sugiyama, S., Skvarca, P., Naito, N., Enomoto, H., Tsutaki, S., Tone, K., Marinsek, S., and Aniya, M.: Ice speed of a calving glacier modulated by small fluctuations in basal water pressure, Nature Geosci, 4, 597–600, https://doi.org/10.1038/ngeo1218, 2011.

495 Sundal, A. V., Shepherd, A., Nienow, P., Hanna, E., Palmer, S., and Huybrechts, P.: Melt-induced speed-up of Greenland ice sheet offset by efficient subglacial drainage, Nature, 469, 521–524, https://doi.org/10.1038/nature09740, 2011.

Thayyen, R. J. and Gergan, J. T.: Role of glaciers in watershed hydrology: a preliminary study of a Himalayan catchment, 4, 115–128, https://doi.org/10.5194/tc-4-115-2010, 2010.

Tsang, L., Durand, M., Derksen, C., Barros, A. P., Kang, D.-H., Lievens, H., Marshall, H.-P., Zhu, J., Johnson, J., King, J., Lemmetyinen, J.,
500 Sandells, M., Rutter, N., Siqueira, P., Nolin, A., Osmanoglu, B., Vuyovich, C., Kim, E., Taylor, D., Merkouriadi, I., Brucker, L., Navari, M., Dumont, M., Kelly, R., Kim, R. S., Liao, T.-H., Borah, F., and Xu, X.: Review article: Global monitoring of snow water equivalent using high-frequency radar remote sensing, The Cryosphere, 16, 3531–3573, https://doi.org/10.5194/tc-16-3531-2022, 2022.

Van Wychen, W., Burgess, D. O., Gray, L., Copland, L., Sharp, M., Dowdeswell, J. A., and Benham, T. J.: Glacier velocities and dynamic ice discharge from the Queen Elizabeth Islands, Nunavut, Canada, Geophysical Research Letters, 41, 484–490,
505 https://doi.org/10.1002/2013GL058558, 2014.

Vincent, C. and Moreau, L.: Sliding velocity fluctuations and subglacial hydrology over the last two decades on Argentière glacier, Mont Blanc area, Journal of Glaciology, 62, 805–815, https://doi.org/10.1017/jog.2016.35, 2016.

Walker, A. E. and Silis, A.: Snow-cover variations over the Mackenzie River basin, Canada, derived from SSM/I passive-microwave satellite data, Annals of Glaciology, 34, 8–14, https://doi.org/10.3189/172756402781817680, 2002.

510 Wang, X., Tolksdorf, V., Otto, M., and Scherer, D.: WRF-based dynamical downscaling of ERA5 reanalysis data for High Mountain Asia: Towards a new version of the High Asia Refined analysis, International Journal of Climatology, 41, 743–762, https://doi.org/10.1002/joc.6686, 2021.

Watson, C., Quincey, D., Carrivick, J., and Smith, M.: The dynamics of supraglacial ponds in the Everest region, central Himalaya, Global and Planetary Change,, 142, 14–27, https://doi.org/10.1016/j.gloplacha.2016.04.008, 2016.

515 Weertman, J.: The Theory of Glacier Sliding, Journal of Glaciology, 5, 287–303, https://doi.org/10.3189/S0022143000029038, 1964.

Wendleder, A., Friedl, P., and Mayer, C.: Impacts of Climate and Supraglacial Lakes on the Surface Velocity of Baltoro Glacier from 1992 to 2017, Remote Sensing, 10, https://doi.org/10.3390/rs10111681, 2018.

Wendleder, A., Lanzenberger, T., and Schmitt, A.: The detection of snow avalanches using TerraSAR-X data, EUSAR 2021; 13th European Conference on Synthetic Aperture Radar, pp. 1–4, 2021a.

520 Wendleder, A., Schmitt, A., Erbertseder, T., D'Angelo, P., Mayer, C., and Braun, M. H.: Seasonal Evolution of Supraglacial Lakes on Baltoro Glacier From 2016 to 2020, Frontiers in Earth Science, 9, https://doi.org/10.3389/feart.2021.725394, 2021b.

Wendleder, A., Mix, V., and Schmitt, A.: The Glacier Zone Index applied on the Manson Icefield, EUSAR 2022; 14th European Conference on Synthetic Aperture Radar, pp. 1–5, 2022.

Werder, M. A., Hewitt, I. J., Schoof, C. G., and Flowers, G. E.: Modeling channelized and distributed subglacial drainage in two dimensions,
525 Journal of Geophysical Research: Earth Surface, 118, 2140–2158, https://doi.org/10.1002/jgrf.20146, 2013.

Østrem, G.: Ice Melting under a Thin Layer of Moraine, and the Existence of Ice Cores in Moraine Ridges, Geographic Annals, 41, 228–230, https://doi.org/10.1007/s00477-018-1605-2, 1959.

Table A1. Pearson correlation of glacier and climate variables for 2017-2019. Only significant correlations according to a 95 % confidence interval are shown.

	Period I 2017 21.03.-04.06.	Period II 2017 05.06.-30.09.	Period I 2018 12.03.-17.07.	Period II 2018 18.07.-30.09.	Period I 2019 27.03.-12.07.	Period II 2019 13.07.–30.09.
Temperature – Snowmelt	0.70	0.81	0.83	0.84	0.80	0.83
Temperature – Supraglacial Lake	0.58	0.71	0.87	0.89	0.70	0.69
Snowmelt – Velocity at Urdukas	0.94	0.30	-0.30	-0.24	-0.21	-0.19
Snowmelt – Velocity at Yermanendu	0.92	0.36	0.08	-0.37	0.09	0.58
Snowmelt – Velocity at Gore	0.93	0.33	0.63	-0.01	0.60	0.69
Snowmelt – Velocity at Concordia	0.92	0.45	0.77	0.36	0.92	0.80
Supraglacial Lake – Velocity at Urdukas	0.91	-0.14	-0.13	-0.09	0.02	-0.42
Supraglacial Lake – Velocity at Yermanendu	0.86	0.48	0.07	-0.28	0.33	0.37
Supraglacial Lake – Velocity at Gore		0.63	0.80	0.12	0.77	0.68
Supraglacial Lake – Velocity at Concordia		0.69	0.93	0.52	0.96	0.87
Precipitation – Velocity at Urdukas	-0.46	-0.05	0.15	0.14	-0.02	0.21
Precipitation – Velocity at Yermanendu	-0.47	-0.53	0.08	0.22	-0.04	0.12
Precipitation – Velocity at Gore	-0.47	0.07	-0.17	0.13	-0.10	0.03
Precipitation – Velocity at Concordia	-0.45	0.07	-0.22	-0.02	-0.14	-0.01
Snowmelt - Runoff-Index	0.80	0.65	0.88	0.93	0.85	0.75
Supraglacial Lake - Runoff-Index	0.72	0.63	0.94	0.90	0.80	0.51
Velocity at Urdukas - Runoff-Index	0.85	-0.12	-0.02	-0.35	-0.03	0.38
Velocity at Yermanendu - Runoff-Index	0.91	-0.03	0.08	-0.48	0.25	0.79
Velocity at Gore - Runoff-Index	0.90	-0.13	0.81	-0.13	0.68	0.64
Velocity at Concordia - Runoff-Index	0.85	-0.04		0.24	0.81	0.57

Table A2. Pearson correlation of glacier and climate variables for 2020-2022. Only significant correlations according to a 95 % confidence interval are shown.

	Period I 2020 21.03.-24.06.	Period II 2020 25.06.-30.09.	Period I 2021 07.03.-19.06.	Period II 2021 20.06.-30.09.	Period I 2022 05.03.-08.07.	Period II 2022 09.07.–30.09.
Temperature – Snowmelt	0.82	0.91	0.78	0.71	0.89	0.90
Temperature – Supraglacial Lake	0.82	0.42	0.76	0.72	0.80	0.89
Snowmelt – Velocity at Urdukas	0.44	0.22	0.73	-0.60	0.59	0.11
Snowmelt – Velocity at Yermanendu	0.68	0.28	0.85	0.26	0.81	0.15
Snowmelt – Velocity at Gore	0.89	0.52	0.84	-0.05	0.86	0.14
Snowmelt – Velocity at Concordia	0.93	0.64	0.89	0.40	0.95	0.32
Supraglacial Lake – Velocity at Urdukas	0.14	0.28	0.51	-0.87	0.36	0.38
Supraglacial Lake – Velocity at Yermanendu	0.44	0.52	0.82	-0.51	0.74	0.55
Supraglacial Lake – Velocity at Gore	0.73	0.72	0.85	-0.38	0.83	0.56
Supraglacial Lake – Velocity at Concordia	0.96	0.60	0.98	0.15	0.86	0.73
Precipitation – Velocity at Urdukas	-0.19	0.17	-0.56	-0.03	-0.22	0.03
Precipitation – Velocity at Yermanendu	-0.26	0.18	-0.53	0.02	-0.32	-0.06
Precipitation – Velocity at Gore	-0.30	0.05	-0.52	0.07	-0.28	-0.06
Precipitation – Velocity at Concordia	-0.29	-0.05	-0.45	0.12	-0.28	-0.06
Snowmelt - Runoff-Index	0.93	0.53	0.79	0.77	0.84	0.82
Supraglacial Lake - Runoff-Index	0.88	-0.11	0.78	0.75	0.75	0.85
Velocity at Urdukas - Runoff-Index	0.50	0.51	0.68	-0.59	0.59	0.25
Velocity at Yermanendu - Runoff-Index		0.22		-0.51	0.79	0.24
Velocity at Gore - Runoff-Index	0.89	-0.15	0.82	-0.36	0.77	0.23
Velocity at Concordia - Runoff-Index	0.94	-0.21	0.82	-0.03		0.38